





Efficient hydrogen evolution reaction due to topological polarization

Ming-Chun Jiang ^{1,2,*}, Guang-Yu Guo,^{1,3} Motoaki Hirayama,^{2,4,†} Tonghua Yu ⁵, Takuya Nomoto ⁶, and Ryotaro Arita ^{5,6}

¹*Department of Physics and Center for Theoretical Physics, National Taiwan University, Taipei 10617, Taiwan*

²*RIKEN Center for Emergent Matter Science, 2-1 Hirosawa, Wako 351-0198, Japan*

³*Physics Division, National Center for Theoretical Sciences, Taipei 10617, Taiwan*

⁴*Quantum Phase Electronics Center, University of Tokyo, Tokyo 113-8656, Japan*

⁵*Department of Applied Physics, University of Tokyo, Tokyo 113-8656, Japan*

⁶*Research Center for Advanced Science and Technology, University of Tokyo, 4-6-1 Meguro-ku, Tokyo, 153-8904, Japan*



(Received 13 July 2022; accepted 3 October 2022; published 21 October 2022)

Materials carrying topological surface states (TSS) provide a fascinating platform for the hydrogen evolution reaction (HER). Based on systematic first-principles calculations for A_3B ($A = \text{Ni, Pd, Pt}$; $B = \text{Si, Ge, Sn}$), we propose that topological electric polarization characterized by the Zak phase can be crucial to designing efficient catalysts for the HER. For A_3B , we show that the Zak phase takes a nontrivial value of π in the whole (111) projected Brillouin zone, which causes quantized electric polarization charges at the surface. There, depending on the adsorption sites, the hydrogen (H) atom hybridizes with the TSS rather than with the bulk states. When the hybridization has an intermediate character between the covalent and ionic bonds, the H states are localized in the energy spectrum, and the change in the Gibbs free energy (ΔG) due to the H adsorption becomes small. Namely, the interaction between the H states and the substrate becomes considerably weak, which is a highly favorable situation for the HER. Notably, we show that ΔG for Pt_3Sn and Pd_3Sn are just -0.066 and -0.092 eV, respectively, which are almost half of the value of Pt.

DOI: [10.1103/PhysRevB.106.165120](https://doi.org/10.1103/PhysRevB.106.165120)

I. INTRODUCTION

Hydrogen evolution reaction (HER) ($2\text{H}^+ + 2\text{e}^- \rightarrow \text{H}_2$) plays a crucial role in renewable energy production for which a variety of experimental and theoretical studies have been performed extensively [1,2]. In the celebrated volcano plot (the plot of the efficiency of an electrocatalytic process as a function of the change in the Gibbs free energy ΔG), the efficiency takes its maximum at $\Delta G \sim 0$ [3–5]. While it has been shown that the elemental Pt is an ideal catalyst as it is at the top of the volcano plot with ΔG being only ~ -0.1 eV [5,6], Pt has a severe limit for widespread industrial usage because of the high cost. Thus, it is an intriguing challenge to search for a replacement for Pt. Recently, it has been proposed that topological materials having surface states with high mobility provide a promising platform to study HER [7–12]. However, the influence of the topological surface states (TSS) on HER is not fully understood, and strategies to predict new candidates are highly desired.

Weyl semimetals such as $1T'$ - MoTe_2 and the TaAs family were recently studied both experimentally and theoretically as potential HER catalysts [13–16]. Also, materials with a large Chern number were predicted and turned out to be exceptional catalysts. For example, high turnover frequencies of 5.6 and 17.1 $\text{H}_2 \text{ s}^{-1}$ were observed for PtAl and PtGa, respectively [17]. From a TSS perspective, Fermi arcs manifested in Weyl

semimetals are characterized by the flow of the Berry curvature between two Weyl points with opposite chirality [18]. Meanwhile, we can also characterize TSS by the Zak phase, which is defined by integrating the Berry connection along a given reciprocal lattice vector. In spinless systems with inversion (\mathcal{P}) and time-reversal (\mathcal{T}) symmetries, a nontrivial $\pi \pmod{2\pi}$ Zak phase signifies topological surface polarization charge if the system is insulating [19]. In contrast to the surface current originating from Fermi arcs in Weyl semimetals, the π Zak phase results in surface dipoles [18,19].

A distinct advantage of topological materials characterized by the π Zak phase is the large size of the relevant region in the projected Brillouin zone (BZ). Even in cases such as PtAl [17] where long Fermi arcs connect with each other at the zone boundary, the phase volume of the Fermi arcs is much smaller than that of the region of the π Zak phase, which covers a large area in the projected BZ [20] and may provide significantly more TSS that are available to assist HER. Indeed, it has been recently shown that some nodal line semimetals such as the TiSi family, PtSn_4 , and VAI_3 [21–23] are promising catalysts. However, the effect of the π Zak phase on HER is still elusive. One reason is that an interchange of 0 and π Zak phase always happens in the projected BZ of nodal line semimetals, which makes the topological polarization less significant. Therefore, while materials for which the π Zak phase lies across the whole projected BZ have yet to be reported, such materials would be an ideal platform to elucidate the role of the topological polarization in HER.

In this paper, we report a nontrivial π Zak phase over the entire (111) projected BZ for a family of topological

*ming-chun.jiang@riken.jp

†hirayama@ap.t.u-tokyo.ac.jp

TABLE I. Experimental lattice constants (a) of bulk A_3B , as well as the optimized bond length A-H and B-H for different adsorption sites (fcc, hcp, and top sites) on 10-layer (111) A_3B substrate. The unit is Å.

Substrate A_3B	a	fcc		hcp		top	
		A-H	B-H	A-H	B-H	A-H	B-H
Pt ₃ Sn	4.004 ^a	1.83	3.32	1.89	3.39	3.73	1.75
Pd ₃ Sn	3.971 ^b	1.79	3.31	1.86	3.37	3.58	1.77
Ni ₃ Sn	3.738 ^c	1.67	3.08	1.73	3.08	3.52	1.77
Ni ₃ Ge	3.571 ^d	1.67	2.99	1.72	3.05	3.25	1.59
Ni ₃ Si	3.500 ^e	1.66	2.98	1.71	3.05	3.09	1.54

^aReference [24].

^bReference [25].

^cReference [26].

^dReference [27].

^eReference [28].

semimetals A_3B (i.e., Pt₃Sn, Pd₃Sn, Ni₃Sn, Ni₃Ge, and Ni₃Si) [24–28], through systematic first-principles calculations. The HER electrocatalytic behavior and its relation to the underlying electronic structure are also investigated. Particularly, we focus on the role of TSS, electronegativity, and bonding formation to unveil possible factors for ideal HER electrocatalysts. It should be noted that the HER of A_3B has not been investigated except for the photocatalytic activity of Pt₃Sn (110) [29].

Intriguingly, the π Zak phase of A_3B covers the whole (111) projected BZ due to the absence of double-band degeneracy near the Fermi level. Also, this topological phase in A_3B is stable due to the charge neutrality of each (111) layer. Previous experiments have indeed shown that the (111) termination plane is closely related to the ideal bulk truncation structure [30,31]. We further confirm that Pt₃Sn and Pd₃Sn are exceptional catalysts for HER in that ΔG is just half of the value of Pt. These results suggest that topological polarization from the π Zak phase can serve as a promising selection for HER catalysts.

The rest of the paper is organized as follows. In Sec. II, a brief description of the crystalline structures of the considered A_3B compounds in conjunction with the theoretical methods and computational details are given. In Sec. III, we look into the electronic structures, including the topology of the A_3B family. Also, we show the calculated adsorption energy (E_{ads}), Gibbs free energy (ΔG), and Bader charge analysis to quantify the catalytic behavior for HER. The possible factors affecting the catalytic behavior are discussed by looking into the role of electronegativity, bond formation, and TSS. Finally, conclusions are presented in Sec. IV.

II. STRUCTURES AND METHODS

This study focuses on the five available experimentally synthesized A_3B compounds, namely, A_3 Sn [24–26], Ni₃Ge [27], and Ni₃Si [28]. All these compounds preserve the cubic symmetry with the space group $Pm\bar{3}m$ (No. 221) with one formula unit per primitive unit cell as illustrated in Fig. 1(a). Table I lists the experimental lattice constants for all five considered systems. To investigate the surface catalytic behavior

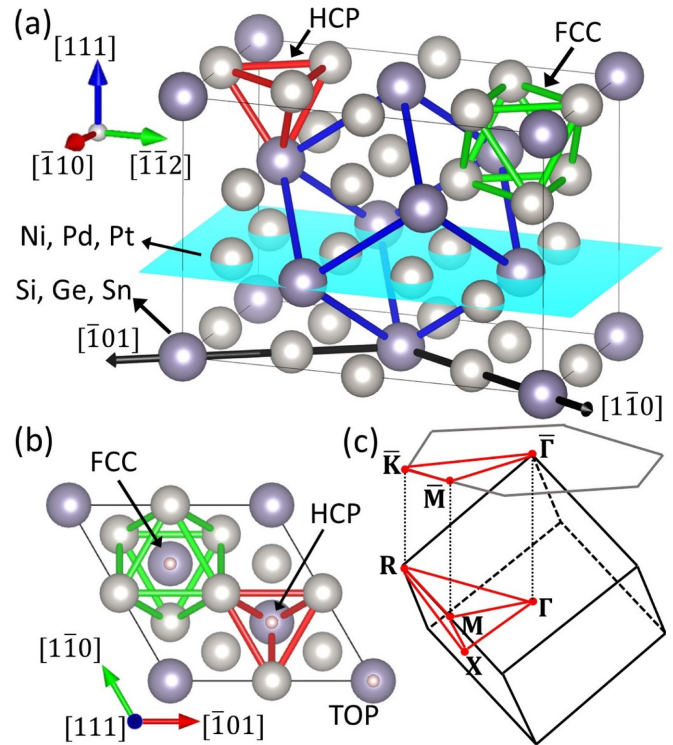


FIG. 1. Crystal structure, adsorption sites, and Brillouin zone of the A_3B family. (a) The lattice structure of A_3B in an orthorhombic supercell. The black vectors show the reduction to a hexagonal supercell. The blue box indicates the primitive cell with the cyan ab facet being the (111) plane of the primitive cell. The red and green bonds form the tetrahedral and octahedral sites, which correspond to the hcp- and fcc-adsorption sites for hydrogen. (b) Stable hydrogen adsorption sites on the (111) surface. (c) Brillouin zone of primitive cell and its projection along the [111] direction. Crystal structures are generated via VESTA [32].

of the A_3B (111) system, we construct a supercell upon the (111) basal planes with cell vectors along $[\bar{1}01]$, $[1\bar{1}0]$, and $[111]$ crystallographic directions, as shown in Figs. 1(a) and 1(b); this supercell forms in a hexagonal lattice, and can be readily extended to a slab along the $[111]$ direction [Fig. 1(b)]. The BZ of the primitive cell and the (111) projected BZ are depicted in Fig. 1(c).

The *ab initio* structural optimization, electronic structures, and free-energy calculation are based on the density functional theory (DFT) with the generalized gradient approximation (GGA) in the form of Perdew-Burke-Ernzerhof (PBE) [33]. The present calculations are performed using the accurate projector-augmented wave method [34] implemented in the Vienna *ab initio* simulation package (VASP) [35,36]. A large plane-wave cutoff energy of 400 eV is used. For the BZ integrations with the tetrahedron method [37], Monkhorst-Pack k meshes of $15 \times 15 \times 15$ and $9 \times 9 \times 1$ are used for the bulk and (111) slab, respectively. The valence orbital set is $6s^15d^9$ for Pt, $5s^14d^9$ for Pd, $4s^13d^9$ for Ni, $4d^{10}5s^25p^2$ for Sn, $3d^{10}4s^24p^2$ for Ge, and $3s^23p^2$ for Si. We study the nontrivial Zak phase and related topological properties of A_3B in the absence of spin-orbit coupling (SOC), based on Wannier functions [38] obtained by WANNIER90 without the iterative

TABLE II. Stretching frequency of hydrogen atom on different adsorption sites (fcc, hcp, and top sites) of the 10-layer (111) A_3B substrate. Stretching directions are parallel (\parallel) or perpendicular (\perp) to the surface. Also, the calculated zero-point energies (ZPE) and the isotropic stretching frequency for hydrogen gas (H_2) are listed. For comparison, we also list the results of hydrogen-adsorbed Pt (111) systems and related studies. Units are meV.

Substrate	fcc			hcp			Top		
	\parallel	\perp	ZPE	\parallel	\perp	ZPE	\parallel	\perp	ZPE
Pt_3Sn	126	121	187	85	136	153	49	211	155
Pd_3Sn	136	115	194	103	127	167	40	201	140
Ni_3Sn	144	119	204	119	128	183	36	202	137
Ni_3Ge	144	133	211	122	146	195	43	222	155
Ni_3Si	142	138	211	119	152	195	40	233	156
Pt	73	150	148				50	281	190
			134 ^a						182 ^a
	Isotropic ZPE								
H_2	515	258							

^aReference [42] (DFT).

maximal-localization procedure [39–41]. We choose the s , p , and d orbitals for A ($A = Ni, Pd, Pt$) and s and p orbitals for B ($B = Si, Ge, Sn$) as the projectors for Wannier functions.

The A_3B (111) slab is modeled with 10 atomic layers and a 14-Å vacuum layer. We use the 1×1 supercell to study the adsorption. Since there is one H atom per formula unit of A_3B on the (111) surface, we define this as a 1-monolayer (ML) coverage of H for the 1×1 supercell [29]. Adsorption occurs on one side of the slab, and the top four metal layers are allowed to relax along with the adsorbate in these calculations. The resulting stable adsorption sites of A_3B (111) are shown in Fig. 1(b), which are the B top site (top adsorption), the A_3 tetrahedral site (hcp adsorption), as well as the A_3 octahedral site (fcc adsorption). The optimized bond length between the adsorbed H and the substrate on different adsorption sites is listed in Table I.

The adsorption energy (E_{ads}) and the difference in the Gibbs free energy ΔG for H adsorption on A_3B (111) are used to evaluate the catalytic behavior toward HER [5,15,23]. The equations go by [5]

$$E_{ads} = \frac{1}{n} \left(E_{slab+H} - E_{slab} - \frac{n}{2} E_{H_2} \right), \quad (1)$$

where n is the number of H atoms, E_{slab+H} , E_{slab} , and E_{H_2} are the total energies of the H atoms adsorbed on the slab, clean slab, and gas phase H_2 , respectively; also,

$$\Delta G = \Delta E_{ads} + \Delta E_{ZPE} - T \Delta S, \quad (2)$$

where E_{ads} is Eq. (1), ΔE_{ZPE} and ΔS are the zero-point energy difference and the entropy difference between the adsorbed H states and the gas phase H_2 , respectively. ΔE_{ZPE} is calculated by the difference in vibrational frequency (ω) of H and gas phase H_2 via $E_{ZPE} = \sum_i \frac{1}{2} \hbar \omega$. Results of stretching frequencies are in Table II. For the entropy difference, due to the small entropy difference between the two phases, we could approximate it by [5]

$$\Delta S \approx -\frac{1}{2} S_{H_2}^0, \quad S_{H_2}^0 = 130.674 \text{ J/Kmol}, \quad (3)$$

where $S_{H_2}^0$ is the standard entropy value of gaseous H_2 at 300 K [43]. Therefore, the $T \Delta S$ is roughly 0.2 eV.

III. RESULTS AND DISCUSSION

A. Electronic structures of A_3B

First of all, we look into the electronic structures of A_3B . As stated in the previous section, A_3B crystallizes in a centrosymmetric simple cubic structure with the space group $Pm\bar{3}m$ (No. 221). Due to the similarity in electron configurations, the same topological properties can be seen for all A_3B materials. Also, the electronegativity of the nickel family and carbon family are close ($Pt = 2.28$, $Pd = 2.2$, $Ni = 1.91$; $Sn = 1.96$, $Ge = 2.01$, $Si = 1.9$ [44]), indicating that covalent bonds may form in A_3B . On the surface, covalent bonds are cut and leave dangling bonds, giving rise to possible surface states. Here, we look into the details of the electronic structure of Pt_3Sn as a representative compound of A_3B .

We calculate the electronic band structure of Pt_3Sn in the absence of SOC, and the results are presented in Fig. 2. First of all, Fig. 2(a) shows the electronic band structure as well as the DOS near the Fermi level of bulk Pt_3Sn . The low DOS and few crossings at the Fermi level suggest a semimetallic nature. Bands around the Fermi level are contributed by the Pt d orbitals with minor contributions of the Sn s and p orbitals. We, therefore, construct the Wannier functions utilizing the mentioned orbitals with the interpolated band structure plotted in dashed red lines in Fig. 2(a). We note that the band structures from DFT and Wannier functions are identical, both of which agree well with previous work in the GGA [45]. Also, due to the \mathcal{PT} symmetry, all bands are Kramers degenerate. Henceforth, we discuss the band degeneracy for one spin channel.

From Fig. 2(a), we notice that on the Γ - R C_{3v} -symmetric line of Pt_3Sn , a nondegenerate band crosses a doubly degenerate band, forming two spinless triple nodal points on Γ and R . The same behavior of splitting arises along the C_{4v} -symmetric lines Γ - X and R - M [46]. In a \mathcal{PT} -symmetric system, doubly degenerate points tend to form in loops, or the so-called nodal lines, characterized by the π Berry phase mechanism and related to the Zak phase mechanism [18]. Interestingly, in the present case, triple nodal points appear and do not form into loops. The split-nodal lines on the zone boundary are also mainly unoccupied. Consequently, we see significant gaps in the BZ outside of the triple nodal points around the Fermi energy [blue and pink gaps in Fig. 2(a)]. This leads us to expect the pink gap to have an identical Zak phase across the whole projected BZ. Our requirement for an ideal platform to study the relation between TSS and the surface reaction is then fulfilled.

Aside from the triple nodal point, in Pt_3Sn , we observe doubly degenerate points along M - Γ , M - X , and M - R lines at $-1.4 \sim -1.5$ eV [circled in green in Fig. 2(a)]. In the BZ, this forms into two loops protected by mirror symmetry of the (110) and (001) planes. As discussed above, we would now expect the Zak phase property originating from the nodal ring around the M point in the blue gap to span across the pink gap and, more importantly, the majority of the Fermi level. To confirm this idea, using the constructed Wannier functions, we

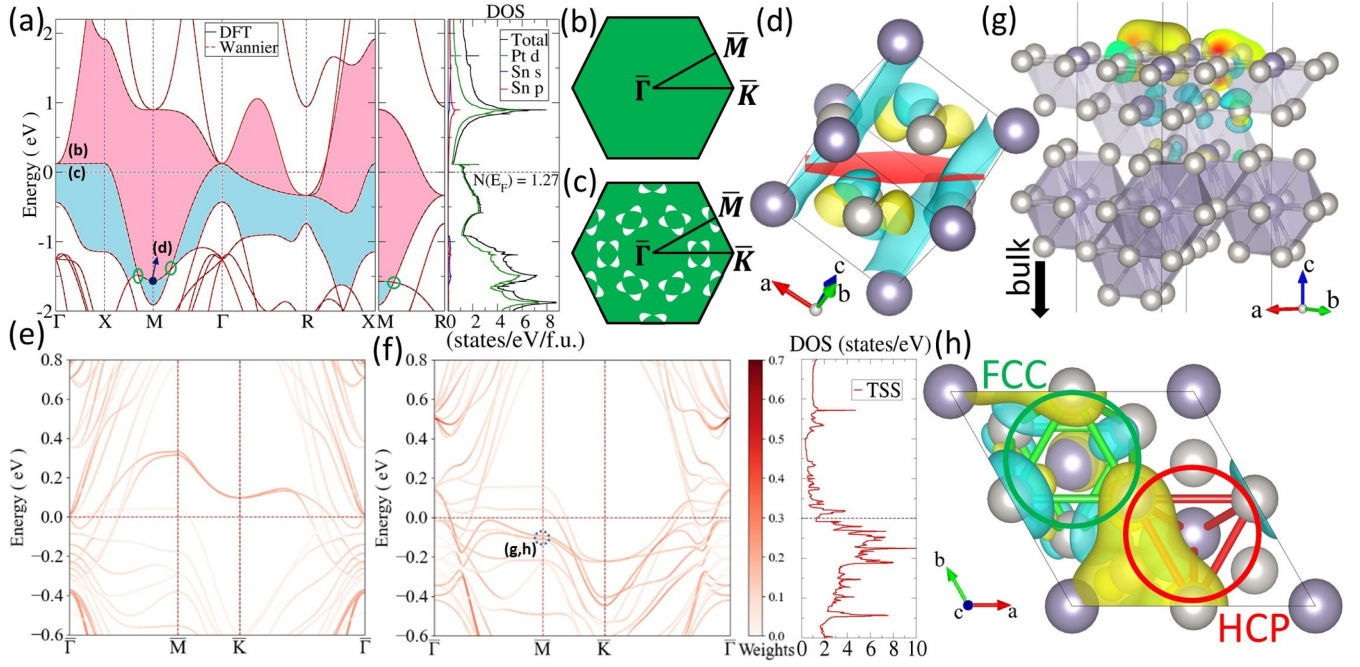


FIG. 2. Electronic structure of Pt_3Sn bulk and (111) slab in the absence of the spin-orbit coupling. (a) Electronic band structure and density of states of bulk Pt_3Sn , with the high-symmetry \mathbf{k} points shown in Fig. 1(c). The calculated Zak phase on the (111) projected Brillouin zone of the (b) pink and (c) blue gap. The green region indicates the π Zak phase. (d) Real bulk wave function of the eigenstate at the time-reversal invariant M point pointed in black in (a). Yellow and blue represent the positive and negative components, respectively. The red slice in the middle indicates the (111) plane. (e), (f) Projected electronic band structure and density of states for the (111) surface of a 10-layer slab of Pt_3Sn in the (e) tight-binding Hamiltonian and (f) the GGA. The color bar indicates the weights of the topological surface state. The Fermi level is set to 0 regarding all band structures. (g), (h) Real wave functions of topological surface state at the \bar{M} point as circled in blue in (f). Yellow and blue represent the positive and negative components, respectively.

calculate the Zak phase by integrating the Berry connection along a reciprocal lattice vector \mathbf{G} . In the case of interest, it is the [111] direction that indicates the surface polarization charge on the (111) plane. The choice of the unit cell will be given in Fig. S1 of the Supplemental Material (SM) [47]. We then calculate the Zak phase as follows:

$$\theta(\mathbf{k}_{\parallel}) = -i \sum_n^{\text{occ.}} \int_0^{|\mathbf{G}|} d\mathbf{k}_{\perp} \langle u_n(\mathbf{k}) | \nabla_{\mathbf{k}_{\perp}} | u_n(\mathbf{k}) \rangle, \quad (4)$$

where $u_n(\mathbf{k})$ is the periodic part of the bulk Bloch wave function. The wave vector \mathbf{k} is decomposed into the component along the lattice vector \mathbf{G} (i.e., \mathbf{k}_{\perp}) and the one perpendicular to \mathbf{G} (i.e., \mathbf{k}_{\parallel}).

The calculated results are given in Fig. 2(b) for the pink gap and (c) for the blue gap in Fig. 2(a). In Fig. 2(b), the Zak phase along the [111] direction is equal to π in the entire projected BZ. This suggests surface polarization charges equal to $e/2$ per surface unit cell on the (111) surface [20]. On the other hand, in Fig. 2(c), we notice patches of 0 Zak phase appearing around 12 centers with, i.e., 6 on \bar{M} . These 12 centers correspond to the 12 M points in the cubic BZ [Fig. 1(c)], and the butterfly-shaped patches are the projections of two nodal rings formed around M [green circles in Fig. 2(a)]. We note that full Zak phase coverage has not been shown in semimetals, although it has been reported in a few insulators such as Sc_2C [20]. Therefore, the A_3B family or, in general, the $Pm\bar{3}m$ space group [46], could be a promising platform to study Zak phase physics in semimetals.

Essentially, the Zak phase represents the Wannier charge center inside a bulk, and a 0 Zak phase indicates an even number of dangling bonds, which leads to an uncertain bulk boundary being of either insulating (bonds connected) or metallic (bonds remain dangling) [19]. To understand the origin of the surface state, we can illustrate the wave function of the bulk eigenstates [20]. Figure 2(d) shows the wave function of the highest valence band at the M point, which is in the gap of interest. We see the Pt $5d$ and Sn p -like orbitals extending across the (111) plane in the middle. This indicates that dangling bonds are formed under a (111) termination. As we stack the slab up, the boundaries at (111) would still have such bonds, which thus cause the surface charge accumulation. Extending the topological bulk property, we determine the origin of the surface state.

Another point of view toward dangling bonds is charge neutrality. That is, the protected surface charges would cause deficiency of the bulk charges. Due to charge conservation, such loss will be compensated by the emerging surface band in a gap for a thick (111) Pt_3Sn slab, which is shown in the slab band structure of the constructed Wannier functions [Fig. 2(e)]. Importantly, in our case, the whole (111) projected BZ has a π Zak phase. This means that the surface band seen in Fig. 2(e) has only this single origin. While the degenerate points occur in Γ and R points of the bulk band structure Fig. 2(a), the surface band at their projection, the $\bar{\Gamma}$ point, would merge with the bulk band. However, the large gap at the X and M points would allow us to observe the highlighted TSS appearing on the high-symmetry \bar{M} and \bar{K} points.

TABLE III. The adsorption energy (E_{ads}), Gibbs free energy (ΔG), and Bader charge analysis of H on different adsorption sites (fcc, hcp, and top sites) of the 10-layer (111) A_3B substrate in the absence of the spin-orbit coupling at room temperature. Also, the Bader charge analysis results of the top-layer atoms are listed with charge differences before and after the adsorption given in the row below. Note that the number of charges for A is the average between the three atoms on the surface.

Substrate A_3B	fcc (eV)					hcp (eV)					Top (eV)				
	E_{ads}	ΔG	H	A	B	E_{ads}	ΔG	H	A	B	E_{ads}	ΔG	H	A	B
Pt ₃ Sn	-0.324	-0.066	1.059	10.342	13.027	-0.606	-0.382	1.067	10.338	13.018	0.828	1.055	1.276	10.377	12.962
	-0.44 ^a		+0.059	-0.048	-0.026			+0.067	-0.051	-0.035			+0.276	-0.012	-0.091
Pd ₃ Sn	-0.356	-0.092	1.099	10.212	13.293	-0.668	-0.430	1.142	10.218	13.263	0.999	1.211	1.297	10.250	13.197
			+0.099	-0.043	-0.021			+0.142	-0.037	-0.052			+0.297	-0.005	-0.118
Ni ₃ Sn	-0.638	-0.363	1.244	10.070	13.602	-0.915	-0.661	1.270	10.071	13.585	0.927	1.136	1.290	10.153	13.446
			+0.244	-0.076	-0.054			+0.270	-0.074	-0.070			+0.290	+0.007	-0.209
Ni ₃ Ge	-0.544	-0.262	1.225	9.991	13.838	-0.978	-0.712	1.262	9.986	13.835	0.823	1.049	1.282	10.067	13.684
			+0.225	-0.071	-0.056			+0.262	-0.076	-0.060			+0.282	+0.005	-0.210
Ni ₃ Si	-0.496	-0.214	1.220	10.022	3.738	-0.991	-0.725	1.249	10.024	3.712	0.630	0.857	1.510	10.115	3.360
			+0.220	-0.076	-0.044			+0.249	-0.075	-0.070			+0.510	+0.016	-0.422
Pt	-0.362	-0.143									-0.391	-0.130			
	-0.39 ^b										-0.42 ^b				

^aReference [48] (DFT).

^bReference [42] (DFT).

With the confirmation of the topological nature of Pt₃Sn, we perform the self-consistent DFT calculation of the slab band structure of a 10-layer (111) Pt₃Sn slab. The result is depicted in Fig. 2(f). By comparing Figs. 2(e) and 2(f), we can see that the TSS merge into the bulk states at an energy level around $-0.1 \sim -0.2$ eV as predicted by the DFT, as clearly shown in the left panel of Fig. 2(f). This is due to the impact of surface charge redistribution, which is adequately treated in DFT but ignored in the calculation based on the Wannier functions. Nonetheless, such TSS still exist in the vicinity of the Fermi level and would contribute to the surface reaction [see the projected density of states shown in the right panel of Fig. 2(f)]. Furthermore, we plot out the real part of the wave function at the time-reversal invariant point \bar{M} of 10-layer Pt₃Sn (111) at Figs. 2(g) and 2(h). We notice that the TSS are contributed mainly by the Pt orbitals with hybridization between the three Pt atoms on the surface. Moreover, the TSS cover the hcp site partially but is repelled from the fcc site, as indicated by the red and green circles, respectively, in Fig. 2(h).

Note that the electronic structures of other A_3B compounds are in Figs. S2–S5 of the SM [47]. The difference in the electronic structure is due to the difference in electronegativity, especially as site A changes. Nevertheless, the π Zak phase on the (111) projected BZ is seen among all A_3B . The resulting TSS are also in the vicinity of the Fermi level [Figs. S2–S5(e) [47]]. It is also essential to point out that the inclusion of SOC would cause a topological phase transition for A_3B to go from a π Zak phase semimetal into a weak Dirac dispersion along [111] direction [45]. Bulk and surface electronic structures in the spinful case are provided in Fig. S6 of the SM [47]. With these, in the Appendix, we discuss the effect of SOC where we show that SOC hardly affects the interaction between the surface states and the H adsorption.

Now that we have shown the topological polarization in Pt₃Sn, we will proceed to the catalytic behavior. The role and the effect of the TSS coverage among different adsorp-

tion sites will be further clarified in Secs. III C and III D, respectively.

B. Catalytic behavior of A_3B

To investigate the catalytic behavior of A_3B , we calculate the E_{ads} as well as the ΔG of H residing at the fcc, hcp, and top sites in the absence of SOC. Results are organized in Table III. First of all, intriguingly, the ΔG of Pt₃Sn and Pd₃Sn (111) fcc adsorption is of value -0.066 and -0.092 eV, respectively. With ΔG roughly half the value of Pt (-0.143 eV), Pt₃Sn and Pd₃Sn are thus prominent HER catalysts with exceptional low ΔG and less or even zero composition of Pt. Second, Ni₃B (111) have ΔG of value around -0.25 eV on the fcc site, larger than that of Pt₃Sn and Pd₃Sn, indicating a worse catalytic behavior. Nevertheless, they are comparable with related theoretical calculations in GGA such as nodal line semimetals PtSn₄ (-0.28 eV) [22], VAl₃ (0.25 eV) [23], or Weyl semimetal TaP (-0.40 eV) [15]. By results of ΔG , we predict the considered A_3B family (Pt₃Sn, Pd₃Sn, Ni₃Sn, Ni₃Ge, Ni₃Si) could be promising catalysts for HER with much less Pt consumption. The calculated results (Table III) agree well with previous studies [42,48].

Among different adsorption sites, the fcc site has the lowest ΔG with a value around $-0.1 \sim -0.3$ eV. Adsorptions on the hcp site have ΔG of value about $-0.4 \sim -0.7$ eV, and the top site behaves the worst in catalysis with ΔG of nearly 1 eV. This indicates that the H atoms are more prone to fcc-site adsorption while being easier to detach simultaneously, which leads to better-performance catalytic behavior. Note that for the fcc and hcp sites, Pt₃Sn and Pd₃Sn have lower ΔG than that of Ni₃B. However, on the top site, the ΔG of Ni₃Si is surprisingly the lowest. This could be attributed to the absence of outer d orbitals in the case of top adsorption, as supported by our results that p orbitals could be better for active sites with only one bond. Still, ΔG of the top site is at least two to four times larger than those of the fcc and hcp sites, which makes it less relevant in the catalytic process. The feature that

TABLE IV. Adsorption energy (E_{ads}), Gibbs free energy (ΔG), bond length, and stretching frequency (ν) of H adsorption on both fcc and hcp sites of 10-layer (111) A_3B substrate in the absence of the spin-orbit coupling at room temperature. Unit of the bond length is Å, and that of the stretching frequency is meV.

Substrate A_3B	fcc+hcp	(eV)	fcc		ν		hcp		ν	
	E_{ads}	ΔG	H-A	H-B		\perp	H-A	H-B		\perp
Pt ₃ Sn	-0.349	-0.101	1.85	3.41	102	126	1.89	3.45	70	140
Pd ₃ Sn	-0.521	-0.211	1.78	3.33	142	110	1.85	3.41	105	131
Ni ₃ Sn	-0.756	-0.428	1.68	3.10	144	113	1.73	3.14	118	131
Ni ₃ Ge	-0.745	-0.400	1.67	3.04	142	134	1.72	3.09	120	147
Ni ₃ Si	-0.742	-0.396	1.67	3.02	140	141	1.71	3.09	117	154

distinguishes the fcc and hcp sites from the top site can be seen in Fig. 2(h). The TSS protected by the nontrivial Zak phase have coverage mostly around the fcc and on the hcp site, suggesting a possible tendency of adsorption sites with TSS having superior catalytic efficiency.

In addition, the effect of the H coverage on the catalytic behavior is small in the case of Pt₃Sn. In Table S1 [47], we show that the ΔG is affected by an order of 0.01 eV when the supercell is extended to 2×1 , which represents the case of a 0.5-ML H coverage. The minor effect of H-H interaction could be due to the distance between H since the diatomic (111) surface leads to less stable active sites. For example, in A_3B , H would migrate from a fcc site of A_2B to A_3 [Fig. 1(b)]. Further discussions are in Note 1 in the SM [47].

Interestingly, in the case of a higher coverage 2 ML, where selectivity comes into play, the ΔG shows significant changes. From Table III, we notice that the E_{ads} of hcp adsorption is lower than fcc adsorption, indicating a stronger H-A bonding strength at the hcp site [5]. This means that the H reconstruction at the hcp site could be slower than the fcc-site HER reaction, implying that the ΔG of the fcc adsorption is worth evaluating in the presence of a preexisting hcp-adsorption (hcp preadsorption). Here, both H atoms and the first four layers are fully relaxed with the same parameters as those in Sec. II. The final results are shown in Table IV. We see that for A_3B , the ΔG of the preadsorption case is in the middle of fcc and hcp adsorption, with energy differences on the order of 0.1 eV. This means that the reaction energy of the fcc adsorption rises under the hcp preadsorption. However, between the hcp adsorption and the double adsorption case, the latter is the catalytically active species [5]. Reversely, when the fcc adsorption happens already, it is harder to go to the double adsorption. In conclusion, we show that the interplay between the fcc site and hcp site plays a significant role in HER. Also, pure fcc adsorption is the most catalytically active reaction, and a reaction coordinate transition from the hcp adsorption to double adsorption is viable.

Finally, we also perform the Bader charge analysis [49] to investigate the charge-transfer behavior, and the results are organized in Table III. Each column beside ΔG shows the number of electrons that belong to the top-layer atoms. The charge difference before and after the adsorption is given in the next row. First, we notice that the H atom tends to receive electrons from A_3B during the adsorption. Second, the H atom that receives fewer electrons shows a propensity for a lower ΔG . For example, the H atom for Pt₃Sn and Pd₃Sn fcc adsorption, with the lowest ΔG , receives only $0.059 e^-$

and $0.099 e^-$, respectively. On the other hand, the H atom of Ni₃B fcc adsorption receives $\sim 0.25 e^-$. In general, the H atom on the fcc site would receive fewer electrons among the same material than that on the top site. Moreover, among the same adsorption sites, the H atom on the Pt₃Sn and Pd₃Sn would also receive fewer electrons than the Ni₃B. From the observations above, we may propose that the conditions of high catalytic performance for the A_3B family are that the H atom interacts with the TSS significantly and receives a small number of electrons from the substrate. We would further incorporate the impact of electronegativity, bonding type, and the TSS in the following subsections based on such an argument.

C. Role of electronegativity and bonding type

The number of electrons transferred during the chemical reaction can be estimated by electronegativity and further classified into different bonding types such as covalent or ionic bonding. From the viewpoint of electronegativity, we notice that for A_3B fcc and hcp adsorptions, the closer the electronegativity for A is to that of H atom (Pt = 2.28, Pd = 2.2, Ni = 1.91, H = 2.2 [44]), the less electrons are donated and the smaller the ΔG gets, which indicates the better the catalytic behavior is. The underlying mechanism is the shifting of the d -band center as interpreted by the ratio of electronegativity between A and H [4,50,51].

A covalent bond is formed if the Bader charge of H remains as $1 e^-$ after the adsorption. Table III shows that, after adsorption, the electrons received by the H atom range from $1.05 e^-$ to $1.5 e^-$, indicating an intermediate bonding between the covalent and ionic. The Sabatier principle [4,52] claims that during an electrocatalytic process, the bonding should neither be too strong nor too weak to avoid difficulty for the reactant to either attach to or detach from the catalysts. Therefore, to understand the bonding character [53,54], we calculate the electron localized function (ELF) for the two cases with the least [Fig. 3(a), Pt₃Sn fcc adsorption, $1.059 e^-$] and most [Fig. 3(b), Ni₃Si top adsorption, $1.510 e^-$] electrons that the H atom obtains. In Fig. 3(a), the ELF appears in the vicinity of the Pt, Sn, and H atoms, suggesting the bonding nature is more of the covalent type. On the other hand, in Fig. 3(b), the electrons are more accumulated around the Si and H atom itself with a hole along the bonding direction. This suggests the bonding nature is more of ionic bonding.

We have shown that the A_3B family forms an intermediate between covalent and ionic bonding after the adsorption

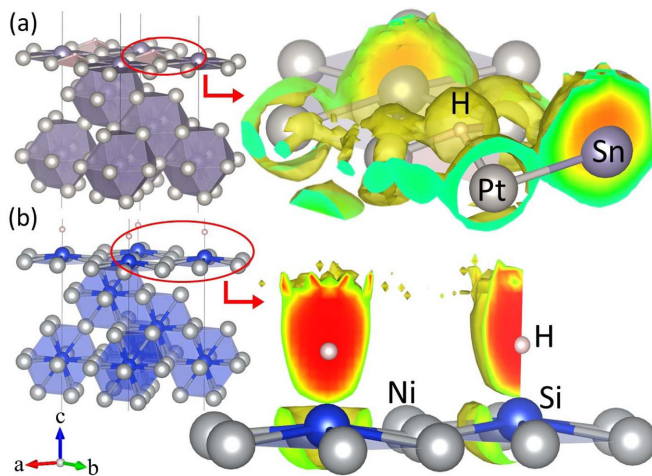


FIG. 3. Electron localized functions for (a) Pt_3Sn (111) fcc adsorption and (b) Ni_3Si (111) top adsorption.

with the degree determined by the electronegativity. While it seems like the more covalent the bonding is, the better the catalytic behavior is for the fcc and hcp sites, the connection to the Sabatier principle is not clear. Therefore, we attempt to elucidate such connections from the band theory point of view. If an atom is weakly attached to a substrate, the overall band structures can be simply viewed as a linear combination of both individual bands.

In Fig. 4(a), the projected band structures of the H atom of the Pt_3Sn (111) fcc adsorption are depicted. First, we notice that the H state is highly localized at an energy level of ~ -8 eV. Such high localization indicates a weak interaction

between Pt_3Sn and the H atom. Also, the bonded H state deeply buried in the spectrum indicates a low d -band center, implying the weakening of adsorption energy by the filling of the anti-bonding state [55]. Second, we further demonstrate the intermediate bonding formation by calculating the band structure of the Pt_3Sn slab with an isolated H_2 molecule, and the results are in Fig. 4(b). The brown line at ~ -5 eV denotes the energy level of the H_2 molecule, which is equivalent to a fully covalent bonding situation. If the energy level of H in the case of $\text{Pt}_3\text{Sn}+\text{H}$ is lower than the case of $\text{Pt}_3\text{Sn}+\text{H}_2$, the bonding of $\text{Pt}_3\text{Sn}+\text{H}$ would be closer to covalent bonding. Indeed, the highlighted states in Figs. 4(a) and 4(b) show a large energy drop, suggesting that the bonding type of $\text{Pt}_3\text{Sn}+\text{H}$ is closer to a covalent pattern. Figure 4(c) is a schematic of the covalent bonding of the H_2 molecule and the intermediate bonding between Pt_3Sn and the H atom. The energy-level difference between Pt_3Sn and H also explains the difference in the weighting of H between the bonding and antibonding state, which is why we observe a strong bonding state of H in Fig. 4(a) in ~ -8 eV but a less clear antibonding state in the higher-energy spectrum in ~ 0.6 eV.

Furthermore, we illustrate the connection between the localization of the H bands and the catalytic behavior by investigating the DOS. Figure 4(d) shows the DOS of the H atom in the cases of Pt_3Sn (111) fcc, hcp, and top adsorptions. From the top panel of Fig. 4(d), we notice the black peak at ~ -8 eV for the fcc adsorption, which is the dark band in Fig. 4(a). Interestingly, unlike fcc adsorption, where no other peaks are shown across the energy spectrum, we see a second prominent peak around -6 eV for hcp adsorption and apparent dispersive bands across the energy spectrum for top adsorption. From the lower panel of Fig. 4(d), the cumulative sum of the DOS is

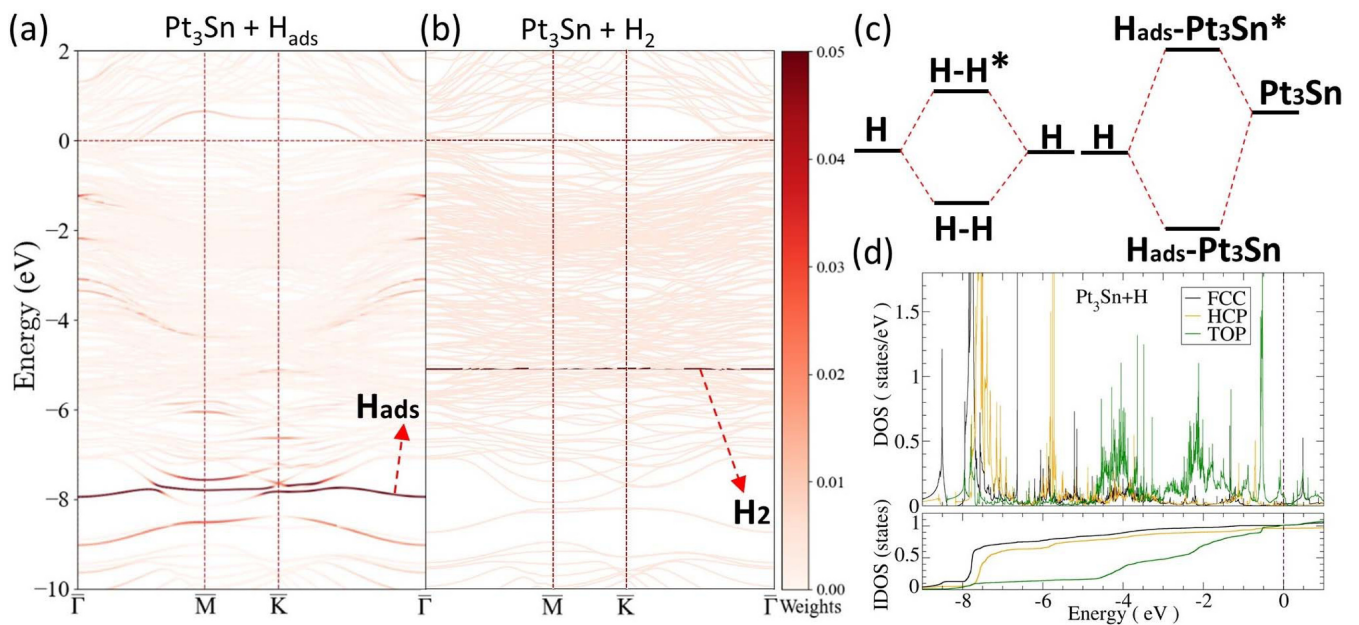


FIG. 4. Bonding between Pt_3Sn (111) and H atom. (a) Band structure of 10-layer Pt_3Sn (111) fcc adsorption highlighted with states projected onto the H atom. (b) Band structure of 10-layer Pt_3Sn (111) with a H_2 molecule sufficiently away from the substrate. The energy level of the H_2 molecule is highlighted in brown. (c) Schematic of covalent bonding and an intermediate between the covalent and ionic bonding. (d) Density of states of the H atom for 10-layer Pt_3Sn (111) fcc, hcp, and top adsorptions. The cumulative sum of the density of states is shown in the lower panel.

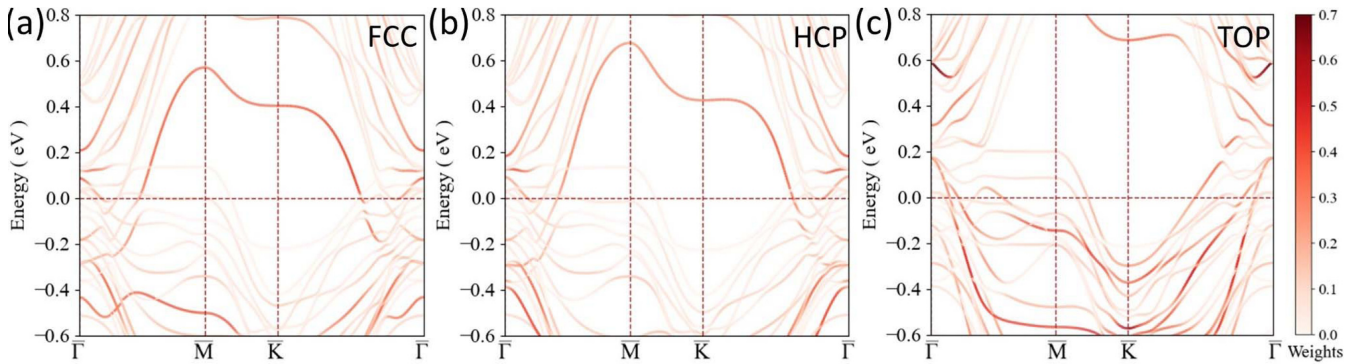


FIG. 5. Surface electronic structures of Pt₃Sn (111) with H adsorption onto the (a) fcc site, (b) hcp site, and (c) top site.

presented. The sharp slope of the black curve indicates the highly localized H bands, while the green curve represents the highly hybridized H bands. Figure S7 [47] shows results for other A_3B , and the slope feature is identical to that of Pt₃Sn. From Table III, the ΔG of the fcc adsorption is the lowest, with the top adsorption being the highest. Therefore, the Sabatier principle is interpreted in the band theory view of point by arguing that the highly localized bands indicate a merely interacting H atom and the slab. This would then lead to better catalytic behavior, as shown from the ΔG calculation.

D. Role of topological surface states

Now we would like to turn our attention back to the role of TSS in the A_3B system. From Table III and Fig. 2(h), we have shown more TSS coverage at the fcc and hcp sites than at the top site and, accordingly, the ΔG of the top site is the largest. In Fig. 5, we calculate the slab band structure of the 10-layer Pt₃Sn (111) fcc, hcp, and top adsorptions. The highlighted states are the TSS, and thus by comparing Figs. 2(f) and 5 we can understand the difference between TSS before and after the adsorption. Also, results of other A_3B are in Figs. S8–S11 [47].

Interestingly, the TSS shift upward from ~ -0.2 eV to an energy level above the Fermi energy and disperses across 0 to 0.6 and 0.8 eV for the fcc and hcp adsorption, respectively [Figs. 5(a) and 5(b)]. The upshift of TSS implies the donation of electrons from the Pt₃Sn substrate to the H atom and, more importantly, the electrons are mainly donated from the TSS. This implication coincides with our Bader charge calculation. For example, from Table III, in the case of Pd₃Sn fcc adsorption, H receives a total amount of 0.099 electrons, which is roughly coming from the top-layer Pd atoms ($-0.129 e^-$). Even in cases with larger ΔG , for example, Ni₃Sn hcp adsorption, H receives 0.270 electrons, which can be covered by the top-layer Ni atoms ($-0.222 e^-$). However, we notice less significant upshifts of the TSS from Fig. 5(c) for the top adsorption. Although the states around -0.2 eV are more localized than before the adsorption, the TSS are less affected than in fcc or hcp adsorption. From the Bader charge analysis (Table III), the number of electrons that H receives during the Pt₃Sn top adsorption is 0.276, which does not fully originate from the top surface ($-0.127 e^-$ in total). This trend appears across all top adsorption of the considered A_3B . Importantly, this indicates that H interacts with the bulk bands on the

sites that underperform the catalytic process. The interaction between the H atom and the bulk bands on the top site also explains the more dispersive and, therefore, more hybridized H DOS in Fig. 4(d).

To have a better understanding, we also plot the TSS after the fcc adsorption of Pt₃Sn and Pd₃Sn, and the results are shown in Figs. S12 and S13 [47]. Note that Fig. S12(a) is the same as Fig. 4(a). Also from Fig. S13(a) [47], we see the localization of the H bands in the deep energy region of Pd₃Sn after the fcc adsorption. Notably, H states and the TSS are also in the upshifted TSS shown in Figs. 5(a) and S8(a), circled on the top of Figs. S12 and S13(a) [47]. Starting from Figs. S12(b) and S12(c) and S13(b) and S13(c) [47], we observe the antibonding formation between H and the TSS. At this particular \bar{M} point, H is mainly interacting with the Pt and Pd atoms indicated in the red arrow in Figs. S12(b) and S12(c) and S13(b) and S13(c) [47]. Note that \bar{M} point would not contain all the symmetry of the material, thus, by C_3 rotational symmetry of A_3B along [111], we would expect such antibonding to appear in-between H and all the surrounding Pt and Pd atoms.

Next, we investigate the bonding formation with H and the TSS after the fcc adsorption. Importantly, now the bands are highly localized, we could then extract the real wave function from the $\bar{\Gamma}$ point [lower circle in Figs. S12(a) and S13(a) [47]]. The results are in Figs. S12(d) and S12(e) and S13(d) and S13(e) [47]. We notice that the TSS form an obvious bonding band with the H atom on the fcc site. The amount of the TSS of this bonding in Figs. S12(d) and S13(d) have a similar amount of charge density, as indicated by the similarity in the blue isosurface area. This echoes with the similarity in E_{ads} of Pt₃Sn and Pd₃Sn for the fcc adsorption in Table III. From Figs. S12(e) and S13(e) [47], the TSS after the fcc adsorption is shown to be still highly localized on the surface. The incoming H atom indeed interacts or exchanges electrons only with the very top surface, making the activation energy of the HER to be very low.

The role of the TSS on HER proposed in this study is illustrated in Fig. 6. From Fig. 6(a), the role of TSS is demonstrated via the case of the fcc and hcp adsorptions in the A_3B family. The π Zak phase in the A_3B covers the whole (111) projected BZ, which guarantees the emergence of the (111) surface dipole. The resulting TSS cover primarily the fcc and hcp sites [Fig. 2(h)]. When the H atom interacts with the TSS [Figs. 5(a) and 5(b)], the resulting catalytic behavior is better

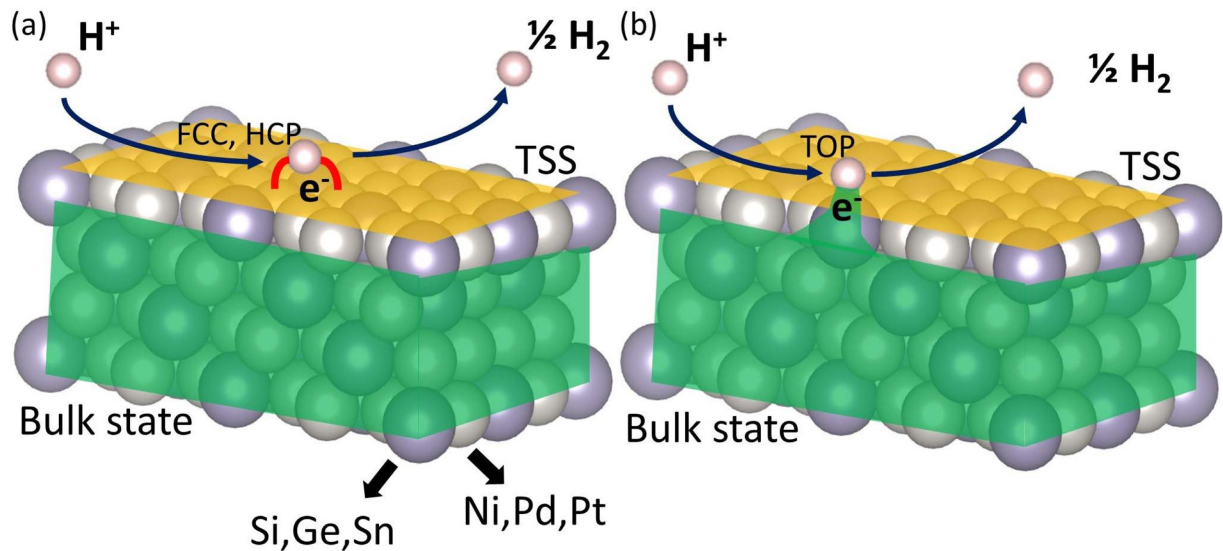


FIG. 6. Schematic plot of interaction between H atom with (a) the topological surface states and (b) the bulk states of the A_3B family.

(Table III) due to the weakly hybridized H bands [Figs. 4(a) and 4(d)] and, accordingly, a weak intermediate between the covalent and ionic bonding is formed. On the other hand, in the case of top adsorption, as illustrated in Fig. 6(b), the catalytic behavior is significantly worsened when the H atom interacts with the bulk bands in Fig. 5(c). The resulting H bands disperse across the energy spectrum as presented in Fig. 4, indicating a stronger hybridization between the substrate and the H atom. This leads to stronger bonding, leading to higher reaction energy needed for the HER. The proposed mechanism suggests that flat H bands are an indicator of suitable catalysts while TSS are good weakly interacting sites. We expect materials with topological polarization characterized by the π Zak phase to be a fruitful platform for future catalysis and surface science studies.

IV. CONCLUSIONS

To summarize, we have investigated the HER behavior and its relation to the underlying electronic structure of topological semimetals A_3B ($A = \text{Ni, Pd, Pt}$; $B = \text{Si, Ge, Sn}$), based on first-principles calculations. First of all, we find that the spinless A_3B family has a nontrivial π Zak phase across the entire (111) projected BZ. The Zak phase originates from a nodal ring around the M point at -1.5 eV, and the lack of doubly degenerate points allows the π Zak phase to span across the whole projected BZ. The TSS appear around ~ -0.2 eV in the slab band structure with real-space surface charges covering partially the hcp site and the rim of the fcc site. Excitingly, the ΔG calculation predicts A_3B to be exceptional catalysts for HER with a very small ΔG value of -0.066 and -0.092 eV for Pt_3Sn and Pd_3Sn fcc adsorption, respectively. This is roughly half the value of the ideal catalyst Pt fcc adsorption (-0.143 eV). The rest, i.e., Ni_3B , have ΔG values around $-0.2 \sim -0.36$ eV, which is comparable with related studies.

By Bader charge analysis, we show that A_3B donates electrons during the H adsorption; accordingly, an intermediate bonding between the covalent and ionic bonding forms. Inter-

estingly, sites and materials with fewer electrons transferred to the H atom tend to obtain lower ΔG . The difference in electronegativity explains such features and indicates that A_3B follows the d -band theory for transition-metal-based catalysts. We can also explain the observations by projected band structures. The DOS spectrum of cases with lower ΔG features sharper H peaks, which indicate flat H bands, rather than dispersive bands across the energy spectrum. From a band-theory perspective, we conclude that the localized H state indicates a weak interaction with the substrate, which is a good indicator according to the Sabatier principle.

Finally, we conclude that fcc and hcp sites outperform the top site due to the existence of TSS and, consequently, stronger topological polarization. We discover that H interacts with TSS on the fcc and hcp sites, and weak covalent bonding is formed, reflected by the flat H bands in the band structure. The above is also supported by plotting the wave function of TSS after the adsorption. On the contrary, the charge transfer of the top site is happening between H and the bulk bands. Once H interacts with the bulk bands, more hybridization between H and A_3B would occur, resulting in larger ΔG . This work first suggests that the A_3B family are rare cases of semimetals to acquire π Zak phase along the whole projected BZ; second, it shows that Zak phase induced topological polarization is a promising platform to study electrocatalysts; third, it introduces a new viewpoint of the Sabatier principle; and finally it unveils the mechanism of TSS toward HER in the A_3B .

ACKNOWLEDGMENTS

The authors thank Y. Miyahara, K. Miyazaki, and H. Kageyama for fruitful discussions throughout this work. M.-C.J. and G.-Y.G. acknowledge the support from the Ministry of Science and Technology and the National Center for Theoretical Sciences (NCTS) of The R.O.C. M.-C.J. and G.-Y.G. are also grateful to the National Center for High-performance Computing (NCHC) for the computing time. M.-C.J. was supported by RIKEN's IPA Program.

TABLE V. The adsorption energy (E_{ads}), Gibbs free-energy difference (ΔG) with spin-orbit coupling at room temperature of H on different adsorption sites (fcc, hcp, and top sites) of the 10-layer A_3B (111) substrate.

Substrate A_3B	fcc		hcp		top	
	E_{ads}	(eV) ΔG	E_{ads}	(eV) ΔG	E_{ads}	(eV) ΔG
Pt ₃ Sn	-0.322	-0.064	-0.572	-0.348	0.798	1.024
Pd ₃ Sn	-0.355	-0.090	-0.667	-0.429	0.993	1.205
Ni ₃ Sn	-0.633	-0.358	-0.909	-0.655	0.929	1.137
Ni ₃ Ge	-0.542	-0.260	-0.972	-0.706	0.826	1.052
Ni ₃ Si	-0.494	-0.212	-0.987	-0.720	0.630	0.857
Pt	-0.335	-0.116			-0.375	-0.115

M.H. acknowledges financial support from JSPS KAKENHI (Grant No. 20K14390) and PRESTO, JST (Grant No. JPMJPR21Q6). T.Y. acknowledges financial support from JSPS KAKENHI Grant No. 22J23068. T.N. acknowledges financial support from PRESTO, JST (Grant No. JPMJPR20L7). R.A. was supported by a Grant-in-Aid for Scientific Research (Grant No. 19H05825) from the Ministry of Education, Culture, Sports, Science, and Technology.

APPENDIX: EFFECT OF SPIN-ORBIT COUPLING

While the Zak phase is defined in the spinless system [56], we would use the conventional Z_2 invariant in spinful systems [57]. When considering the SOC, which is large in Pt-based systems, the topological phase of A_3B will shift from a π Zak phase to a weak Dirac dispersion along the [111] direction [Z_2 invariant (0,111)] [45] due to the gap opening at Γ and R points [Fig. S6(a)]. In Fig. S6(b) [47], we see the slab band structure of the constructed Wannier functions

with SOC. Compared to Fig. 2(e), surface bands have split Kramers degeneracy at all \mathbf{k} points except the time-reversal invariant point \bar{M} . Among the four split bands in Fig. S6(b), due to their existing in a gap, SOC would not affect the existence of surface bands around the Fermi level. The charge compensation mentioned in Sec. III A would force the surface band to appear and reside inside a gap and this argument does not require the inclusion of spin.

Furthermore, DFT results are given in Fig. S6(c) [47] and, similar to the spinless case [Fig. 2(d)], surface bands merge into bulk bands and surface states are hidden around the Fermi level. Interestingly, the band dispersion before and after the Pt₃Sn fcc adsorption is not highly affected by the SOC [compare Fig. 2(f) to 5(a) and compare Fig. S6(c) to S6(d)]. This indicates that the hidden surface states still interact with the H atoms and thus the SOC plays a negligible role. The existence of surface states guaranteed by the nontrivial π Zak phase plays a significant role in the current scenario. Accordingly, in Table V, we look into the effect of the SOC on the catalytic behavior by calculating ΔG with SOC included.

First of all, we note that the calculated vibrational frequency with or without the SOC is close. Therefore, the changes in the resulting ΔG would mainly come from the changes in E_{ads} . From Table V, generally, the ΔG becomes smaller when SOC is considered. Based on the compounds, the difference, due to the atomic number, is roughly 4.5%, 0.9%, 0.7%, 0.4%, 0.5%, and 15% for Pt₃Sn, Pd₃Sn, Ni₃Sn, Ni₃Ge, Ni₃Si, and Pt, respectively. In the previous paragraph, we argued the interaction between surface states and the H atom is insignificantly affected by the SOC. Here, from Table V, we can see that the SOC effect on catalytic behavior is roughly in the order of 10 meV, while the difference among adsorption sites is in the order of 100 meV (Tables III and V). Thus, we conclude that the proposal regarding the role of TSS is still valid in the case of A_3B when considering the SOC.

- [1] J. A. Turner, Sustainable hydrogen production, *Science* **305**, 972 (2004).
- [2] M. Monai, M. Melchionna, and P. Fornasiero, From metal to metal-free catalysts: Routes to sustainable chemistry, in *Advances in Catalysis* Vol. 63, edited by C. Song (Academic, New York, 2018), Chap. 1, pp. 1–73.
- [3] B. Hammer and J. Nørskov, Theoretical Surf Sci and catalysis–calculations and concepts, in *Advances in Catalysis* Vol. 45 (Academic, New York, 2000), pp. 71–129.
- [4] B. Li, W. Gao, and Q. Jiang, Electronic and geometric determinants of adsorption: Fundamentals and applications, *J. Phys. Energy* **3**, 022001 (2021).
- [5] J. K. Nørskov, T. Bligaard, A. Logadottir, J. R. Kitchin, J. G. Chen, S. Pandelov, and U. Stimming, Trends in the exchange current for hydrogen evolution, *J. Electrochem. Soc.* **152**, J23 (2005).
- [6] S. Trasatti, Work function, electronegativity, and electrochemical behaviour of metals, *J. Electroanal. Chem. Interfacial Electrochem.* **39**, 163 (1972).
- [7] J. Xiao, L. Kou, C.-Y. Yam, T. Frauenheim, and B. Yan, Toward rational design of catalysts supported on a topological insulator substrate, *ACS Catal.* **5**, 7063 (2015).
- [8] Q. Xu, G. Li, Y. Zhang, Q. Yang, Y. Sun, and C. Felser, Descriptor for hydrogen evolution catalysts based on the bulk band structure effect, *ACS Catal.* **10**, 5042 (2020).
- [9] L. M. Schoop, F. Pielhofer, and B. V. Lotsch, Chemical Principles of Topological Semimetals, *Chem. Mater.* **30**, 3155 (2018).
- [10] G. Li and C. Felser, Heterogeneous catalysis at the surface of topological materials, *Appl. Phys. Lett.* **116**, 070501 (2020).
- [11] H. Chen, W. Zhu, D. Xiao, and Z. Zhang, CO Oxidation Facilitated by Robust Surface States on Au-Covered Topological Insulators, *Phys. Rev. Lett.* **107**, 056804 (2011).
- [12] L. Li, J. Zeng, W. Qin, P. Cui, and Z. Zhang, Tuning the hydrogen activation reactivity on topological insulator heterostructures, *Nano Energy* **58**, 40 (2019).
- [13] D. Lu, X. Ren, L. Ren, W. Xue, S. Liu, Y. Liu, Q. Chen, X. Qi, and J. Zhong, Direct vapor deposition growth of 1T' MoTe₂ on carbon cloth for electrocatalytic hydrogen evolution, *ACS Appl. Energy Mater.* **3**, 3212 (2020).
- [14] U. Gupta and C. Rao, Hydrogen generation by water splitting using MoS₂ and other transition metal dichalcogenides, *Nano Energy* **41**, 49 (2017).
- [15] C. R. Rajamathi, U. Gupta, N. Kumar, H. Yang, Y. Sun, V. Süß, C. Shekhar, M. Schmidt, H. Blumtritt, P. Werner, B. Yan,

- S. Parkin, C. Felser, and C. N. R. Rao, Weyl semimetals as hydrogen evolution catalysts, *Adv. Mater.* **29**, 1606202 (2017).
- [16] R. Ghosh, M. Singh, L. W. Chang, H.-I. Lin, Y. S. Chen, J. Muthu, B. Papnai, Y. S. Kang, Y.-M. Liao, K. P. Bera, G.-Y. Guo, Y.-P. Hsieh, M. Hofmann, and Y.-F. Chen, Enhancing the photoelectrochemical hydrogen evolution reaction through nanoscrolling of two-dimensional material heterojunctions, *ACS Nano* **16**, 5743 (2022).
- [17] Q. Yang, G. Li, K. Manna, F. Fan, C. Felser, and Y. Sun, Topological engineering of pt-group-metal-based chiral crystals toward high-efficiency hydrogen evolution catalysts, *Adv. Mater.* **32**, 1908518 (2020).
- [18] M. Hirayama, R. Okugawa, and S. Murakami, Topological semimetals studied by ab initio calculations, *J. Phys. Soc. Jpn.* **87**, 041002 (2018).
- [19] M. Hirayama, R. Okugawa, T. Miyake, and S. Murakami, Topological Dirac nodal lines and surface charges in fcc alkaline earth metals, *Nat. Commun.* **8**, 14022 (2017).
- [20] M. Hirayama, S. Matsuiishi, H. Hosono, and S. Murakami, Electrides as a New Platform of Topological Materials, *Phys. Rev. X* **8**, 031067 (2018).
- [21] J. Li, H. Ma, Q. Xie, S. Feng, S. Ullah, R. Li, J. Dong, D. Li, Y. Li, and X.-Q. Chen, Topological quantum catalyst: Dirac nodal line states and a potential electrocatalyst of hydrogen evolution in the TiSi family, *Sci. China Mater.* **61**, 23 (2018).
- [22] G. Li, C. Fu, W. Shi, L. Jiao, J. Wu, Q. Yang, R. Saha, M. E. Kamminga, A. K. Srivastava, E. Liu, A. N. Yazdani, N. Kumar, J. Zhang, G. R. Blake, X. Liu, M. Fahlman, S. Wirth, G. Auffermann, J. Gooth, S. Parkin *et al.*, Dirac nodal arc semimetal PtSn_4 : An ideal platform for understanding surface properties and catalysis for hydrogen evolution, *Angew. Chem. Int. Ed.* **58**, 13107 (2019).
- [23] X.-P. Kong, T. Jiang, J. Gao, X. Shi, J. Shao, Y. Yuan, H.-J. Qiu, and W. Zhao, Development of a Ni-Doped VA13 Topological Semimetal with a Significantly Enhanced HER Catalytic Performance, *J. Phys. Chem. Lett.* **12**, 3740 (2021).
- [24] I. R. Harris, M. Norman, and A. W. Bryant, A study of some palladium-indium, platinum-indium and platinum-tin alloys, *J. Less-Common Met.* **16**, 427 (1968).
- [25] O. Woo, J. Rezek, and M. Schlesinger, X-ray diffraction analyses of liquid-phase sintered compounds of Pd_3Sn and Ni_3Sn , *Mater. Sci. Eng.* **18**, 163 (1975).
- [26] J. F. Cannon, Effect of high pressure on the structures of AB₃-type layered compounds. (ICSD# 105353), *Mater. Res. Soc. Symp. Proc.* **22**, 113 (1984).
- [27] T. Suzuki, Y. Oya, and S. Ochiai, The mechanical behavior of nonstoichiometric compounds Ni_3Si , Ni_3Ge , and Fe_3Ga , *Metall. Trans. A* **15**, 173 (1984).
- [28] A. Morozkin, A. Knotko, A. Garshev, V. Yapaskurt, R. Nirmala, S. Quezado, and S. Malik, The Ce-Ni-Si system as a representative of the rare earth-Ni-Si family: Isothermal section and new rare-earth nickel silicides, *J. Solid State Chem.* **243**, 290 (2016).
- [29] J. Yao, Y. Zheng, X. Jia, L. Duan, Q. Wu, C. Huang, W. An, Q. Xu, and W. Yao, Highly Active $\text{Pt}_3\text{Sn}\{110\}$ -Excavated Nanocube Cocatalysts for Photocatalytic Hydrogen Production, *ACS Appl. Mater. Interfaces* **11**, 25844 (2019).
- [30] A. N. Haner, P. N. Ross, and U. Bardi, The surface structure and composition of the low index single crystal faces of the ordered alloy Pt_3Sn , *Catal. Lett.* **8**, 1 (1991).
- [31] A. H. Haner, P. N. Ross, U. Bardi, and A. Atrei, Surface composition determination of Pt-Sn alloys by chemical titration with carbon monoxide, *J. Vac. Sci. Technol. A* **10**, 2718 (1992).
- [32] K. Momma and F. Izumi, VESTA 3 for three-dimensional visualization of crystal, volumetric and morphology data, *J. Appl. Crystallogr.* **44**, 1272 (2011).
- [33] J. P. Perdew, K. Burke, and M. Ernzerhof, Generalized Gradient Approximation Made Simple, *Phys. Rev. Lett.* **77**, 3865 (1996).
- [34] P. E. Blochl, Projector augmented-wave method, *Phys. Rev. B* **50**, 17953 (1994).
- [35] G. Kresse and J. Hafner, Ab initio molecular dynamics for liquid metals, *Phys. Rev. B* **47**, 558 (1993).
- [36] G. Kresse and J. Furthmuller, Efficient iterative schemes for ab initio total-energy calculations using a plane-wave basis set, *Phys. Rev. B* **54**, 11169 (1996).
- [37] O. Jepsen and O. Anderson, The electronic structure of h.c.p. Ytterbium, *Solid State Commun.* **88**, 871 (1993).
- [38] Q. Wu, S. Zhang, H.-F. Song, M. Troyer, and A. A. Soluyanov, WannierTools: An open-source software package for novel topological materials, *Comput. Phys. Commun.* **224**, 405 (2018).
- [39] N. Marzari and D. Vanderbilt, Maximally localized generalized Wannier functions for composite energy bands, *Phys. Rev. B* **56**, 12847 (1997).
- [40] I. Souza, N. Marzari, and D. Vanderbilt, Maximally localized Wannier functions for entangled energy bands, *Phys. Rev. B* **65**, 035109 (2001).
- [41] G. Pizzi, V. Vitale, R. Arita, S. Blügel, F. Freimuth, G. Géranton, M. Gibertini, D. Gresch, C. Johnson, T. Koretsune, J. Ibañez-Azpiroz, H. Lee, J.-M. Lihm, D. Marchand, A. Marrazzo, Y. Mokrousov, J. I. Mustafa, Y. Nohara, Y. Nomura, L. Paulatto *et al.*, Wannier90 as a community code: New features and applications, *J. Phys.: Condens. Matter* **32**, 165902 (2020).
- [42] T. T. T. Hanh, Y. Takimoto, and O. Sugino, First-principles thermodynamic description of hydrogen electroadsorption on the Pt(111) surface, *Surf. Sci.* **625**, 104 (2014).
- [43] M. Chase, *NIST-JANAF Thermochemical Tables*, 4th ed. (American Institute of Physics, 1998).
- [44] S. S. Zumdahl, *Chemical Principles*, 5th ed. (Houghton Mifflin, Boston, 2004), Chap. 13.2, pp. 587–590.
- [45] M. Kim, C.-Z. Wang, and K.-M. Ho, Coexistence of type-II Dirac point and weak topological phase in Pt_3Sn , *Phys. Rev. B* **96**, 205107 (2017).
- [46] K.-H. Ahn, W. E. Pickett, and K.-W. Lee, Coexistence of triple nodal points, nodal links, and unusual flat bands in intermetallic APd_3 ($A=\text{Pb}, \text{Sn}$), *Phys. Rev. B* **98**, 035130 (2018).
- [47] See Supplemental Material at <http://link.aps.org/supplemental/10.1103/PhysRevB.106.165120> for Figs. S1– S13, Table S1, and Supplemental Note 1.
- [48] P. Liu, A. Logadottir, and J. Nørskov, Modeling the electrooxidation of CO and H_2/CO on Pt, Ru, PtRu and Pt_3Sn , *Electrochim. Acta* **48**, 3731 (2003).
- [49] W. Tang, E. Sanville, and G. Henkelman, A grid-based Bader analysis algorithm without lattice bias, *J. Phys.: Condens. Matter* **21**, 084204 (2009).
- [50] H. Xu, D. Cheng, D. Cao, and X. C. Zeng, A universal principle for a rational design of single-atom electrocatalysts, *Nat. Catal.* **1**, 339 (2018).
- [51] W. Gao, Y. Chen, B. Li, S.-P. Liu, X. Liu, and Q. Jiang, De-

- termining the adsorption energies of small molecules with the intrinsic properties of adsorbates and substrates, *Nat. Commun.* **11**, 1196 (2020).
- [52] P. Sabatier, *La catalyse en chimie organique* (Liège, Librairie polytechnique, Paris, 1920).
- [53] A. D. Becke and K. E. Edgecombe, A simple measure of electron localization in atomic and molecular systems, *J. Chem. Phys.* **92**, 5397 (1990).
- [54] B. Silvi and A. Savin, Classification of chemical bonds based on topological analysis of electron localization functions, *Nature (London)* **371**, 683 (1994).
- [55] Y. Zheng, Y. Jiao, M. Jaroniec, and S. Z. Qiao, Advancing the electrochemistry of the hydrogen-evolution reaction through combining experiment and theory, *Angew. Chem. Int. Ed.* **54**, 52 (2015).
- [56] J. K. Asbóth, L. Oroszlány, and A. Pályi, *A Short Course on Topological Insulators: Band Structure and Edge States in One and Two Dimensions* Vol. 919 (Springer, Cham, 2016).
- [57] L. Fu, C. L. Kane, and E. J. Mele, Topological Insulators in Three Dimensions, *Phys. Rev. Lett.* **98**, 106803 (2007).